

An improvement of the Space-Time Image Velocimetry combined with a new denoising method for estimating river discharge

Haoyuan Zhao^a, Hua Chen^{a,*}, Bingyi Liu^a, Weigao Liu^a, Chong-Yu Xu^b, Shenglian Guo^a, Jun Wang^a

^a State Key Laboratory of Water Resources and Hydropower Engineering Science, Wuhan University, Wuhan, China

^b University of Oslo, Oslo, Norway



ARTICLE INFO

Keywords:
STIV
Flow measurement
Image analysis
Filtering technology

ABSTRACT

The Space-Time Image Velocimetry (STIV) is a time-averaged velocity measurement method, which takes river surface images as the analysis object, and detects the Main Orientation of Texture (MOT) in a generated Space-Time Image (STI) to obtain one-dimensional velocities on the water surface. The STIV has great potential in real-time monitoring of river flow owing to its high spatial resolution and low time complexity. However, the generated STI contains a lot of noise and interference texture, which is inevitable in practical applications. The practicality of the STIV is severely limited by the low-quality STI. To solve this problem, a denoising method based on the filtering technology is proposed and combined with different texture detection algorithms in this paper. The accuracy of this method is verified through a comparative field experiment with an impellor-style current meter. The experimental results show: (1) By using this new denoising method, the robustness and accuracy of the STIV are significantly improved no matter what kind of texture detection algorithm is adopted; (2) Among all the texture detection algorithms, the FFT-based STIV combined with the new denoising method performs best. The relative errors of the surface velocities are controlled within 6%, and the relative errors of the discharges are controlled within $\pm 4\%$.

1. Introduction

Due to global climate changes in recent years, there is growing evidence that disasters caused by floods occur more frequently in the world from small to large river basins [1]. Therefore, in terms of flood forecasting and risk management, water resources management, and hydrology research, it is more urgent to obtain the velocity distribution, the peak flow discharge, and discharge changes in high flood periods, especially in extreme cases [2–4]. At present, discharge is typically estimated from in situ measurements of flow velocity by using current meters, floats, or Acoustic Doppler Current Profilers (ADCPs). However, it is very hard to obtain discharge data quickly, timely, and accurately through these methods in emergent flood events. Current meters have been widely used to estimate mean flow velocity, but this method is time-consuming and laborious [5]. Thus, for rivers with short flood transit time, it is impossible to precisely capture the peak flow information by using this method. Besides, as an intrusive method, submerging a current meter in the water is almost impossible in a high flood

period [6]. The float is another widely-used instrument in hydraulic measurement since it is cheap and easy in terms of field operation. However, its accuracy is questionable when floats are trapped by vortices generated in a flood and it is very hard to put floats on the water surface when the bridge is inundated by a very large flood. ADCPs have emerged as an important measuring tool since the 1990s [7]. However, there will be a large deviation or, even an error in the measurement results of ADCPs in the case of high turbulence, aeration, and bed movements. What's more, ADCPs cannot always be used from an economic view.

To solve the above problems, the non-intrusive surface flow velocity measurement technique based on the image analysis has emerged in the past decades. This technique can measure surface velocity distributions safely and conveniently by analyzing video images captured from the river surface. The idea behind the use of video images is that visible surface flow features composed of surface ripples or floating objects are advected with the surface velocity as long as the wind effect is negligible. According to the different methods used for estimating the surface

* Corresponding author.

E-mail address: chua@whu.edu.cn (H. Chen).

velocity, this technique can be divided into two types: The Large-Scale Particle Image Velocimetry (LSPIV) and the Space-Time Image Velocimetry (STIV). The LSPIV is an improvement of the Particle Image Velocimetry (PIV) technology used in laboratory fluid mechanics research. It uses natural floats or water surface patterns as water flow tracers, the natural light as the main light source, a digital camera or a video camera as image acquisition equipment, and obtains the two-dimensional flow velocity field by matching images of tracers in the analysis area [8]. This method has been applied to the observation of the surface flow and the estimation of the discharge in many different circumstances [9–16]. However, the LSPIV has some shortcomings: First, it relies heavily on the visibility of tracers, but the visibility of flow tracers is poor in the natural environment due to complex optical conditions [17]; Second, there are many uncertainties in the selection of the analysis area size. If the size of the analysis area is large, the spatial resolution of the measurement will be reduced due to the spatial average effect [18]. On the contrary, if the analysis area is small, it is easy to be mismatched due to the lack of target information [19]. Third, it requires a large storage memory to save hundreds of large-sized images and a powerful CPU to calculate coefficients for the pattern matching, which undoubtedly increases the cost of the measurement. Chickadel et al. [20] first used space-time data collected from short-time series of a video to analyze nearshore surface currents. Fujita et al. [21] applied this idea to measure the cross-sectional velocity distribution in a river and named this method the Space-Time Image Velocimetry (STIV). The STIV is designed to build the Space-Time Image (STI) which comes from tracking the variation of brightness along a velocity-measuring line in successive multiple images. Based upon the STIs, the STIV estimates the MOT in the image and calculates the one-dimensional velocity of each velocity-measuring line. Given that many velocity-measuring lines are simultaneously set along a cross-section, the horizontal distribution of streamwise velocity can be obtained to calculate the cross-sectional discharge. The STIV was proved to be a better method than the LSPIV in discharge measurement. Rather than using the image match in the LSPIV, the STIV is almost ten times faster than the LSPIV to obtain the same amount of information [21], except that the LSPIV is a two-dimensional measurement method whereas the STIV is a one-dimensional measurement method in the streamwise direction. Therefore, the STIV is not suitable for measuring the circulated or the unsteady flow which varies its direction with time, but suitable for the discharge measurement which only needs the unidirectional velocity distribution along a cross-section. Because of the above characteristics, the STIV has been used for flood discharge measurement in various specified field conditions with success and was developed into a software KU-STIV [22–24]. At the same time, various texture detection algorithms have been proposed, such as the Gradient Tensor Method (GTM) [21], the Two-Dimensional Autocorrelation Function Method (QUESTA) [25], and the FFT-based STIV (FFT) [26].

In practical applications, illumination changes, standing surface waves, the shadow of background projected on the water surface, obstacles, raindrops, etc., greatly affect the quality of the generated STIs. A variety of methods have been proposed to reduce the influence of noise: (1) Method based on the weighted average of different regions [21]. The STI is divided into several local windows. Then, the coherence value is introduced to reflect the clarity of the texture in each local window. By this means, the influence of the regions with unclear texture can be eliminated; (2) Method based on the standardization (STD) filter [25]. The STD filter is developed to equalize the unevenly distributed image intensity included in the STIs and make them much clearer by normalizing the image through the standard deviation of each vertical pixel array; (3) Method based on the edge recognition [26]. Edge information is used to reflect the orientation of the texture and suppress the low-frequency noise component. However, these methods cannot effectively reduce or eliminate the influence of noise and interference texture (this will be discussed in detail in section 2.2 of this paper). The low-quality STIs with noise and interference texture are not appropriate

for texture detection by using the GTM, the QUESTA, or the FFT. To solve this problem, a denoising method based on the filtering technology is proposed in this paper, which can filter out the noise and interference texture in the STIs. Then, this denoising method is combined with three texture detection algorithms and its performance is evaluated through a comparative experiment conducted at a hydrological station with the impellor-style current meter.

Before introducing the newly proposed method, it is necessary and meaningful to introduce different versions of the STIV and analyze their defects in detail, since they are good starting points to new developments. In the following sections, after a brief introduction of the STIV, the need for a new denoising method is motivated by studying the problems of existing texture detection algorithms. The development and evaluation of the new method are then presented, followed by a discussion of experimental results and possible future developments.

2. The STIV and its problems

2.1. Outline of the STIV

When the STIV is applied to flow measurement, video images are taken from the river bank and several velocity-measuring lines are set parallel to the flow direction. Then, the brightness information of each velocity-measuring line in consecutive surface images is extracted to form the STI. This procedure is demonstrated clearly in Fig. 1 (a). The panels in Fig. 1 (a) are used as the Ground Control Points (GCP) for image rectification and camera calibration [27]. In the STI, as shown in Fig. 1 (b), the horizontal axis refers to the length of the velocity-measuring line, and the vertical axis represents the duration time of the video.

From the STI, the brightness evolution of a velocity-measuring line can be seen clearly. If the distance of surface flow features moving along the velocity-measuring line is L meters in T seconds in the physical coordinate system, it corresponds to l pixels in k frames in the STI, as shown in Fig. 1 (b). Thus, the time-averaged velocity of the velocity-measuring line can be calculated as:

$$v = \frac{L}{T} = \frac{l \cdot S_x}{k \cdot S_t} = \tan \alpha \cdot \frac{S_x}{S_t} = \tan \alpha \cdot S_x \cdot \text{fps} \quad (1)$$

where S_x (m/pixel) is the resolution of the velocity-measuring line, S_t (Sec/pixel) is the unit time scale of the time axis, α (degree) is the MOT of the STI, and fps (pixel/Sec) denotes frames per second of the camera used.

In the current versions of the STIV, there are three algorithms to calculate the MOT: The Gradient Tensor Method (GTM), the Two-Dimensional Autocorrelation Function (QUESTA), and the FFT-based STIV (FFT). Different algorithms adopt different methods to reduce the influence of image noise:

2.1.1. GTM

In the GTM, the STI is first divided into several local windows. Coherency C of each window is introduced to evaluate the clarity of the texture. With the increase of texture clarity, the value of C also increases. When the orientation and the coherency of all windows are worked out, it is possible to calculate the mean orientation angle by taking the coherency C as the weight (see in Fig. 2). Thus, windows with clear orientation information will get higher weights, while windows with an anisotropic gray-level structure will get lower weights. By this means, the influence of the regions with unclear texture can be eliminated.

2.1.2. QUESTA

In the QUESTA, the image is enhanced by the STD filter:

$$I^S(x, t) = [I(x, t) - \mu_t(x)] / \sigma_t(x) \quad (2)$$

where $I(x, t)$ is the original gray-level intensity of the STI, $I^S(x, t)$ is the

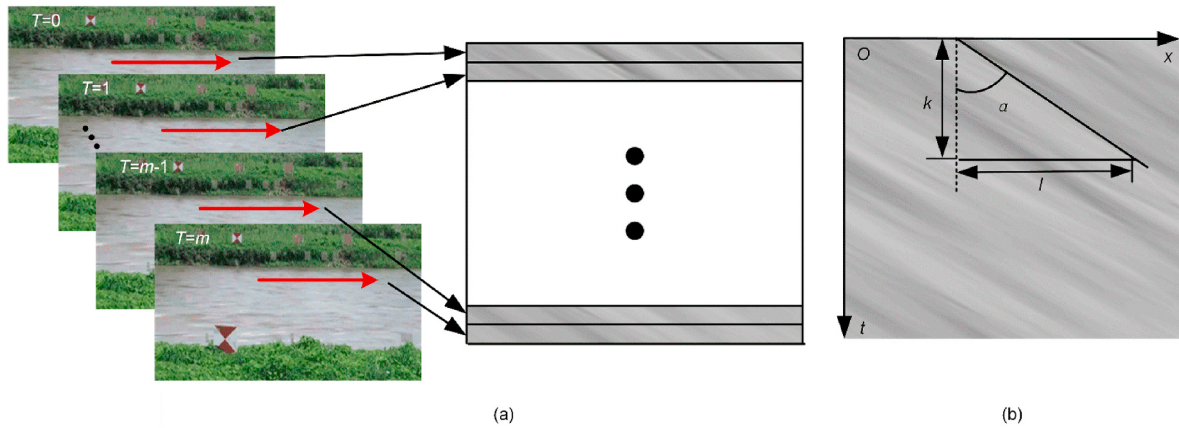


Fig. 1. Generation of the STI. (a) The process of the STI generation. The red line with an arrow represents the velocity-measuring line set along the flow direction. The black and white panels represent the ground control points. $T = 0$ represents the first frame of the video and so on. (b) The generated STI of the velocity-measuring line indicated in (a). (For interpretation of the references to colour in this figure legend, the reader is referred to the Web version of this article.)

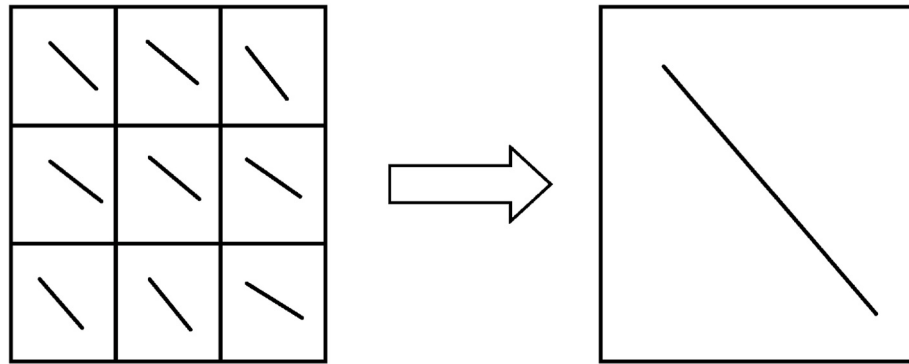


Fig. 2. The process of calculating the mean orientation angle in the GTM. The left represents the orientation vectors in each local window and the right is the mean orientation angle for this STI.

filtered image, $\mu_t(x)$ is the mean value of pixel intensity of a vertical array and $\sigma_t(x)$ is the standard deviation of this pixel array.

The STD filter is developed to equalize the unevenly distributed image intensity included in the STIs and make them much clearer by normalizing the image through the standard deviation of each vertical pixel array.

2.1.3. FFT

In the FFT, the edge of the texture is used for spectrum transform instead of the original STI to enhance the accuracy of the MOT detection. Because the edge information can reflect the orientation of the texture and suppress the low-frequency noise component. The Canny operator is

used to get a binary image of the edge, as shown in Fig. 3.

The surface velocity can be calculated out according to Eq 1 when the MOT is obtained by one of the above three algorithms. Then, the discharge can be calculated by converting the surface velocity to the depth-averaged velocity through the surface velocity coefficient η_s :

$$\eta_s = \frac{m}{m+1} \quad (3)$$

where m is the roughness coefficient. Table 1 shows the value of η_s in different cases:

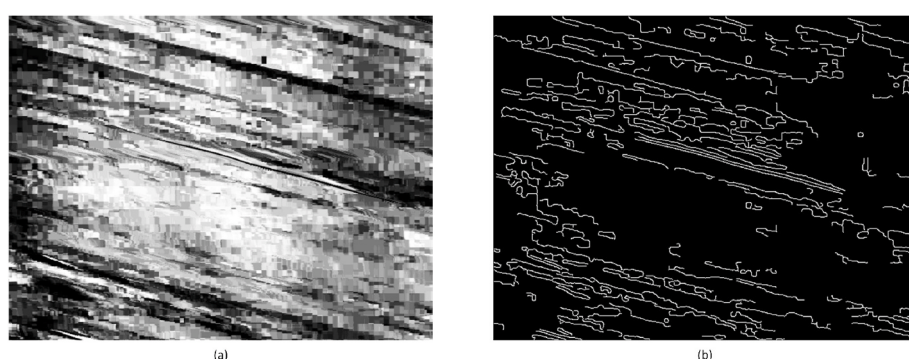


Fig. 3. The edge of the texture. (a) The original STI. (b) The STI after edge detection.

Table 1

Estimate of the surface velocity coefficient.

	Normal	Smooth	Rough	Very rough
m	5–7	8–10	3–4	1–2
η_s	0.83–0.88	0.89–0.91	0.75–0.8	0.5–0.67

2.2. Problems in current algorithms

2.2.1. Disturbance of noise and interference texture

To illustrate the problem better, we use six examples for analysis in the following parts. Unlike in an ideal laboratory flume, many factors are uncontrollable in the natural environment, which greatly affects the quality of the generated STIs. For example, the illumination changes, standing surface waves, the shadow of background projected on the water surface, obstacles, or the falling rain may introduce noise and interference texture into the STIs. Fig. 4 shows STIs obtained in six typical cases: 1) normal, 2) obstacle, 3) wave, 4) shadow, 5) light, 6) rain. These STIs are acquired in various rivers, whose original image sizes are different, but they are transformed to the same size for comparison here. It can be seen from Fig. 4 that the STIs obtained in the other five cases contain noise and interference texture except for the normal case. The reasons why the noise occurs can be inferred from the name given to each STI in Fig. 4. For example, obstacle refers to the case where obstacles, such as vegetation or rock, obstruct the view of the camera; Wave refers to the situation where a large wave passes through a river during video shooting; Light refers to the case where the sunlight changes during video shooting; Rain refers to the situation that raindrops drop on the river surface. When the shooting conditions are good in the daytime, a uniform texture as shown in the normal case can be obtained.

2.2.1.1. GTM. In the GTM, only the clear orientation information is picked out by referring to the coherence value and used to calculate the mean MOT of the entire STI. However, this method can only evaluate the clarity of image patterns, but cannot eliminate image noise. More importantly, the method has no effect when noise interference is so strong that the whole image presents anisotropy. Table 2 shows the comparison between the calculated values by the GTM and the true values of the MOTs in the six cases above (the window used in each STI is a square with the side length of 15 pixels).

As can be seen from Table 2, when the image does not contain interference texture (the normal case), texture recognition using the GTM achieves a good result. When the image contains noise and interference texture, there will be a large deviation. For example, the relative error is as high as 239.17% in the obstacle case.

The STI obtained in the shadow case will be taken as an example to explain the reason: when the side length of the window is 15 pixels, the whole image is divided into 336 windows. The distributions of the coherency and the orientation angle of these 336 windows are shown in Fig. 5. As can be seen from Fig. 5, the coherency values are all below 0.55, and the proportion of windows whose coherency values are under 0.2 is as high as 81.5%, indicating that the texture of all windows exhibits severe anisotropy due to the noise interference. Besides, the

Table 2

Comparison of the calculated values by the GTM and true values in six cases.

Case	True value (°)	Calculated value by the GTM (°)	Relative error
Normal	71.2	72.6	1.97%
Obstacle	12.0	40.7	239.17%
Wave	71.7	65.2	-9.07%
Shadow	57.1	47.0	-17.69%
Light	17.6	43.7	148.30%
Rain	61.3	55.8	-8.97%

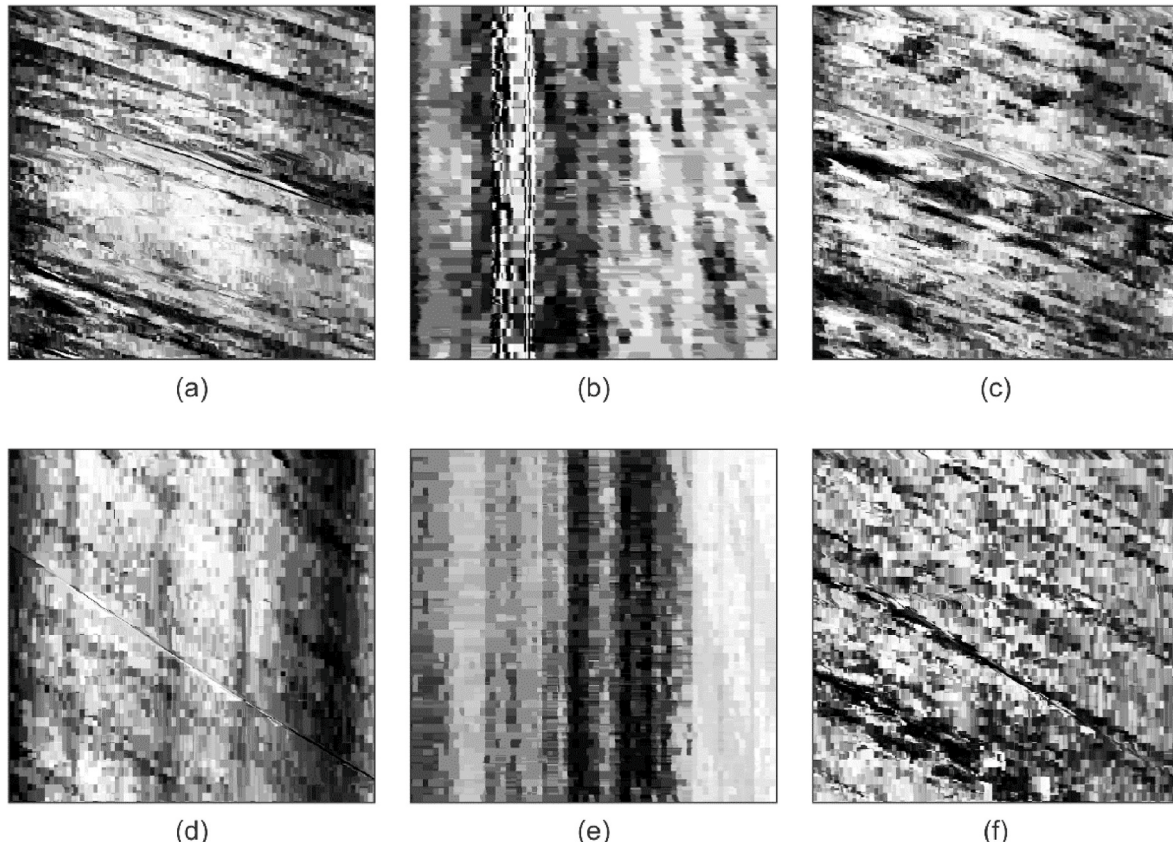


Fig. 4. STIs obtained in different cases. (a) normal. (b) obstacle. (c) wave. (d) shadow. (e) light. (f) rain.

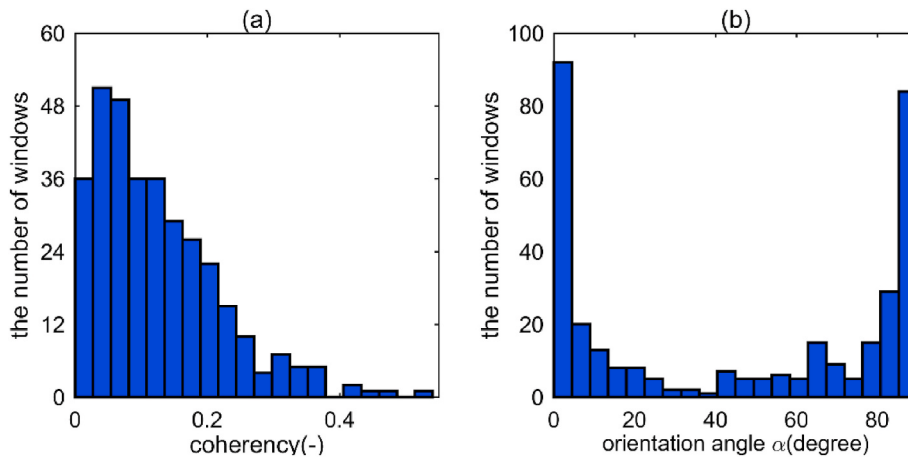


Fig. 5. Distributions of the coherency and the orientation angle by using the GTM in the shadow case.

windows with MOTs below 10° and above 80° account for 34.82% and 35.12%, respectively, which results from the stripy texture parallel to the t axis and the blocky texture on the right side of the image. At the same time, the windows with MOTs within the error limit of 10% ($51.4^\circ \sim 62.8^\circ$) only account for 8%. It is also worth noting that because the noise is clear and obvious in this STI, windows containing interference texture get higher weights when we calculate the average angle. Instead, windows containing true information get lower weights. All the above reasons lead to the deviation of calculation results and indicate that it is not appropriate to use the GTM to identify images that contain noise.

2.2.1.2. QESTA. To eliminate interference patterns extending in the t axis direction (such as the obstacle case, the shadow case, and the light case), the STD filter is proposed in the QESTA. Fig. 6 shows the results of applying this filter to these six cases.

As shown in Fig. 6, the vertical stripe patterns have been removed, and the texture representing the flow has become clear in the shadow case, the light case, and the obstacle case. Table 3 shows the comparison between the calculated values by the QESTA and the true values of the

Table 3

Comparison of the calculated values by the QESTA and true values in six cases.

Case	True value ($^\circ$)	Calculated value by the QESTA ($^\circ$)	Relative error
Normal	71.2	70.0	-1.68%
Obstacle	12.0	28.9	140.83%
Wave	71.7	77.4	7.95%
Shadow	57.1	58.4	2.28%
Light	17.6	30.7	74.43%
Rain	61.3	65.1	6.20%

MOTs in the six cases above (the coefficient of intensification M used here is 15).

Because the STD filter eliminates the noise in the vertical direction, the relative errors of recognition results are reduced compared with the GTM. However, the STD filter cannot eliminate interference patterns in other directions, so the calculation error caused by noise still exists.

2.2.1.3. FFT. In the FFT, the edge of the texture is used for spectrum transform instead of the original STI to enhance the accuracy of the MOT

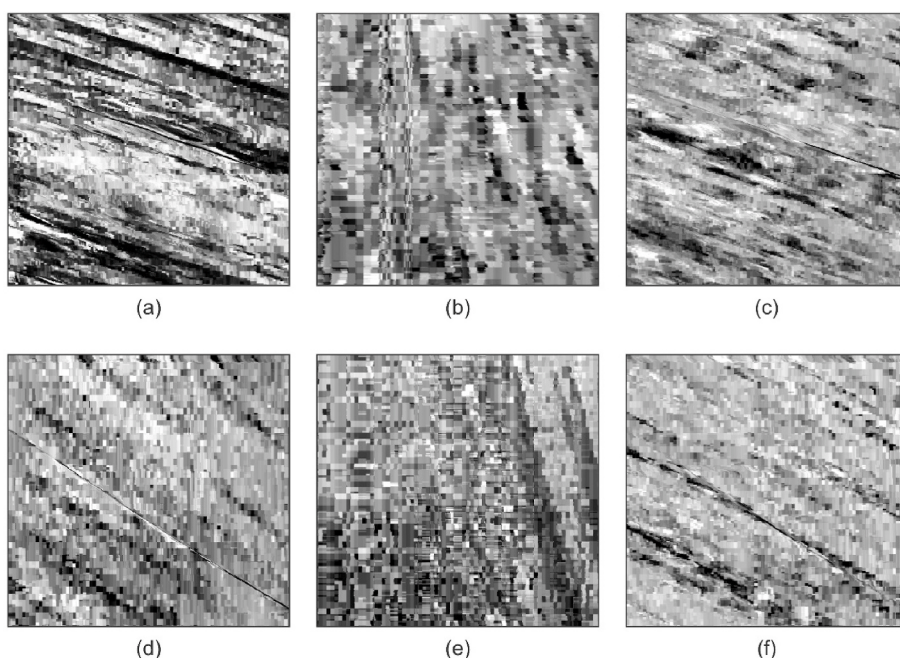


Fig. 6. Filtered STIs with the STD filter in six cases. (a) normal. (b) obstacle. (c) wave. (d) shadow. (e) light. (f) rain.

detection. The edge detection results of these six STIs are shown in Fig. 7.

As can be seen from Fig. 7, except for the normal and wavy cases, the Canny operator fails to detect the edge of the MOT. We can also see that when the quality of the STI is low, two serious problems arise: First, the edge of the texture is seriously deformed, lacking stable and reliable geometric features; Second, the edge of interference texture is also detected, which greatly affects the accuracy of the results. When we transform the edge detection results of the case (b), (d), (e), and (f) into the frequency domain by using Fourier transform, we find that the results of the Main Orientation of Spectra (MOS) are wrong. Thus, the texture orientation angle cannot be calculated.

In summary, these three algorithms have serious problems in texture detection, because of their ineffectiveness in dealing with the deteriorated STIs. Therefore, there has been strong anticipation to develop a new algorithm that can enhance the quality of the STI.

2.2.2. Uncertainty of parameter values

As parameters in the GTM and the QUESTA, the values of the side length of the window and the coefficient of intensification M have a very important influence on the calculation results. In the GTM, the value of the side length of the window used in the previous study is 15 pixels [23] and the value of the intensification coefficient M is 15 in the QUESTA [25]. However, such values are empirical and have no scientific basis. Fig. 8 shows the calculated values with different sizes of the window and different M by using the GTM and the QUESTA respectively. (The size of the window is from 10 pixels to 60 pixels with the step of 5, and M is from 10 to 20 with the step of 1). At the same time, the relative error of each calculated value is also given in Fig. 8.

As can be seen from Fig. 8, different values of parameters lead to different results of the same image. In the GTM, the difference between the maximum angle and the minimum angle is 8.4° , and the difference is 5.6° in the QUESTA. Besides, when the window size is 10 pixels and M is 16, the results of these two methods are closest to the true value, which is different from the values recommended by previous studies. So, the optimal value of the parameter is not invariable but varies with the characteristics of the image. However, there are few solutions to choose the optimal values of these parameters in the practical application. So strictly speaking, the results obtained by these two methods are unreliable because of the uncertainty of the parameter values.

3. A new denoising method

3.1. Window function filtering

To avoid the signal break caused by the periodicity of the Fourier series, we first filter the original STI in the spatial domain before transforming it into the frequency domain. In order not to introduce new parameters into the algorithm, the Hanning window function [28] is chosen in this study.

First, two one-dimensional Hanning functions $\mathbf{W}(m)$ and $\mathbf{W}(n)$ are obtained according to the dimensions M and N of the STI $I(m, n)$:

$$\begin{cases} \mathbf{W}(n) = \frac{1}{2} \left[1 - \cos\left(2\pi \frac{n}{N}\right) \right], & 0 \leq n \leq N \\ \mathbf{W}(m) = \frac{1}{2} \left[1 - \cos\left(2\pi \frac{m}{M}\right) \right], & 0 \leq m \leq M \end{cases} \quad (4)$$

Secondly, these two one-dimensional window functions are synthesized into a two-dimensional window function $\mathbf{W}(m, n)$:

$$\mathbf{W}(m, n) = \mathbf{W}(m)^T \times \mathbf{W}(n) \quad (5)$$

Finally, the original STI $I(m, n)$ is filtered by the two-dimensional window function $\mathbf{W}(m, n)$ to obtain the filtered STI $I'(m, n)$:

$$I'(m, n) = \mathbf{W}(m, n)^* I(m, n) \quad (6)$$

The original STI and the processed STI are shown in Fig. 9.

3.2. Detection of the principal direction of the Fourier spectrum

In the new method, the Fourier spectrum of the STI processed by the window function is obtained by using the two-dimensional discrete Fourier transform (2-D DFT). Let $f(x, y)$ for $x = 0, 1, 2, \dots, M-1$ and $y = 0, 1, 2, \dots, N-1$ denote a digital image of size $M \times N$ pixels. The 2-D DFT of $f(x, y)$, denoted by $F(u, v)$, is given by the equation [28]:

$$F(u, v) = \sum_{x=0}^{M-1} \sum_{y=0}^{N-1} f(x, y) \exp\left[-j2\pi\left(\frac{ux}{M} + \frac{vy}{N}\right)\right] \quad (7)$$

for $u = 0, 1, 2, \dots, M-1$ and $v = 0, 1, 2, \dots, N-1$. We could expand the exponential into sine and cosine functions, with the variables u and v determining their frequencies (x and y are summed out). The frequency domain is the coordinate system spanned by $F(u, v)$ with u and v as frequency variables. This is analogous to the spatial domain which is the coordinate system spanned by $f(x, y)$ with x and y as spatial variables. Even if $f(x, y)$ is a real function, its transform $F(u, v)$ is complex in

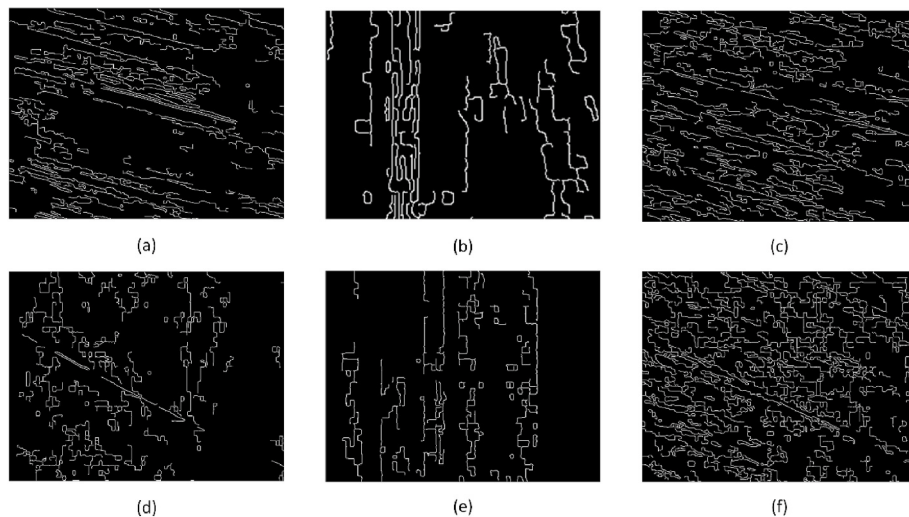


Fig. 7. STIs after edge detection in six cases. (a) normal. (b) obstacle. (c) wave. (d) shadow. (e) light. (f) rain.

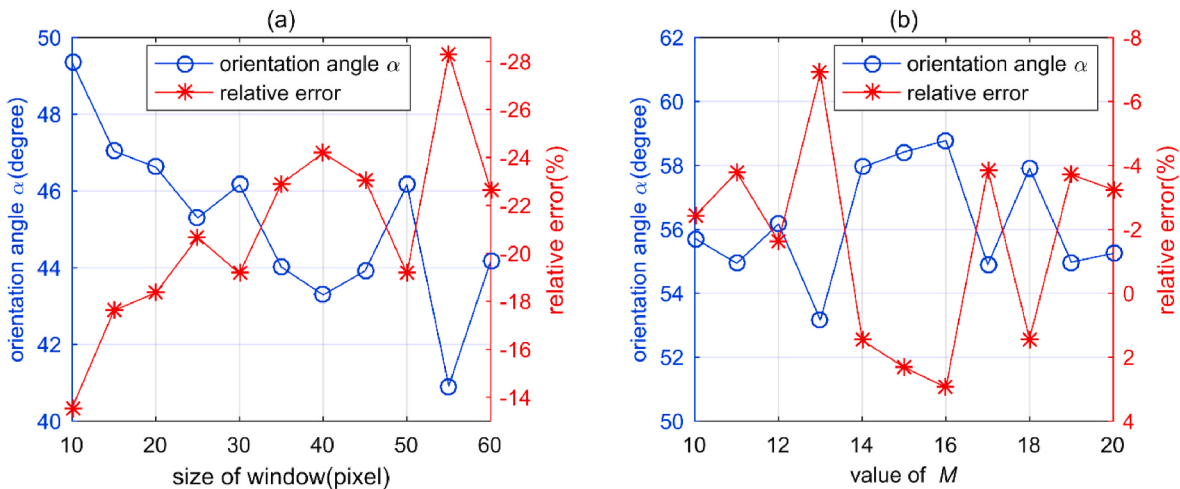


Fig. 8. (a) Calculated values with different sizes of the window by using the GTM (shadow case). (b) Calculated values with different M by using the QESTA (shadow case).

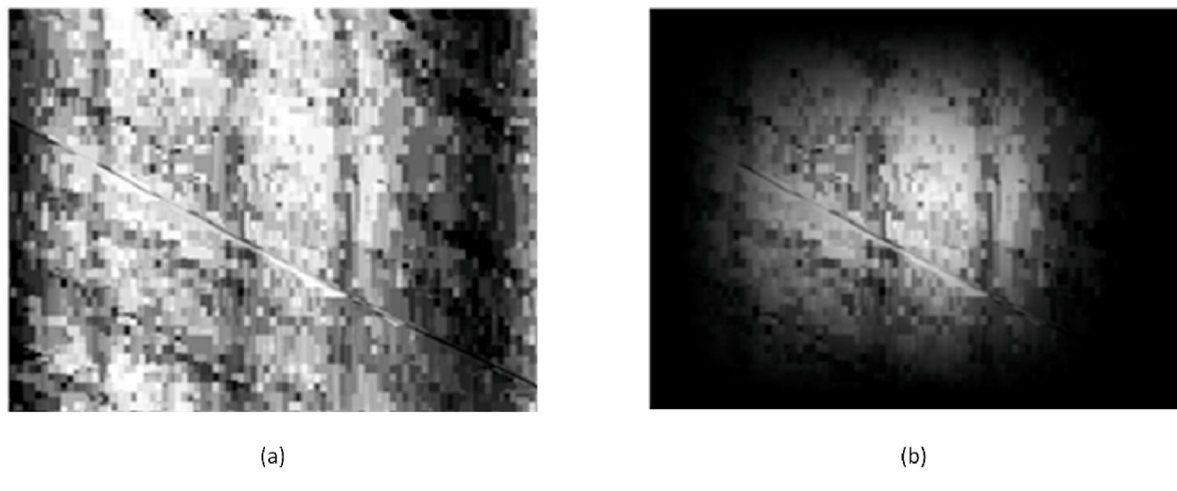


Fig. 9. Window function filtering. (a) Original STI. (b) STI processed by the window function.

general. The principal method for analyzing a transform visually is to compute its spectrum and display it as an image. Letting $R(u, v)$ and $I(u, v)$ represent the real and imaginary components of $F(u, v)$, the Fourier spectrum is defined as

$$|F(u, v)| = [R^2(u, v) + I^2(u, v)]^{\frac{1}{2}} \quad (8)$$

As an example, an original STI in the spatial domain and the Fourier spectrum of the processed STI are shown respectively in Fig. 10 (a) and Fig. 10 (b).

It can be seen from Fig. 10 (a) and Fig. 10 (b) that the textures in the processed STI are superimposed together in the frequency domain and form a spectral line passing through the center of the Fourier spectrum, which is called the auto-registration property of the Fourier transform. The auto-registration property refers to that objects of the same shape in the spatial domain, regardless of their positions, will be superimposed together to form a spectral line that passes through the center of the Fourier spectrum [29]. The direction of the spectral line is called the principal direction of the Fourier spectrum.

To obtain the principal direction of the Fourier spectrum, the distribution of the spectrum in Fig. 10 (b) is transformed into the polar coordinate (ρ, θ) shown in Fig. 10 (c). Then, the values of $|F(\theta)|$ are calculated in the semicircle space of $0\text{--}180^\circ$ according to Eq. (9).

$$|F(\theta)| = \int_0^{\max(\rho)} |F(\rho, \theta)| d\rho \quad (9)$$

At last, the maximum value of $|F(\theta)|$ is searched in the semicircle space. To be specific, the search is conducted with a step of 1° , and the result is denoted as θ . The angle θ that maximizes $|F(\theta)|$ is defined as the principal direction of the Fourier spectrum:

$$\theta = \arg \max |F(\theta)| \quad (10)$$

This process is shown in Fig. 10 (d) and the Fourier spectrums of the STIs in Fig. 4 are shown in Fig. 11. What should be particularly pointed out is that due to the interference of noise and the limitation of search accuracy, θ obtained in this step is a rough value, which is used to determine the filtering range in the subsequent step.

3.3. Image filtering in the frequency domain

In general, image filtering in the spatial domain often involves complex convolution operations, and if the image is converted into the frequency domain via the 2-D DFT, the complex convolution operations would become simple multiplication operations. In the STI, the texture pattern contains most of the high-frequency components, while the uniform background contains most of the low-frequency components. Based on the idea of preserving the texture as much as possible while

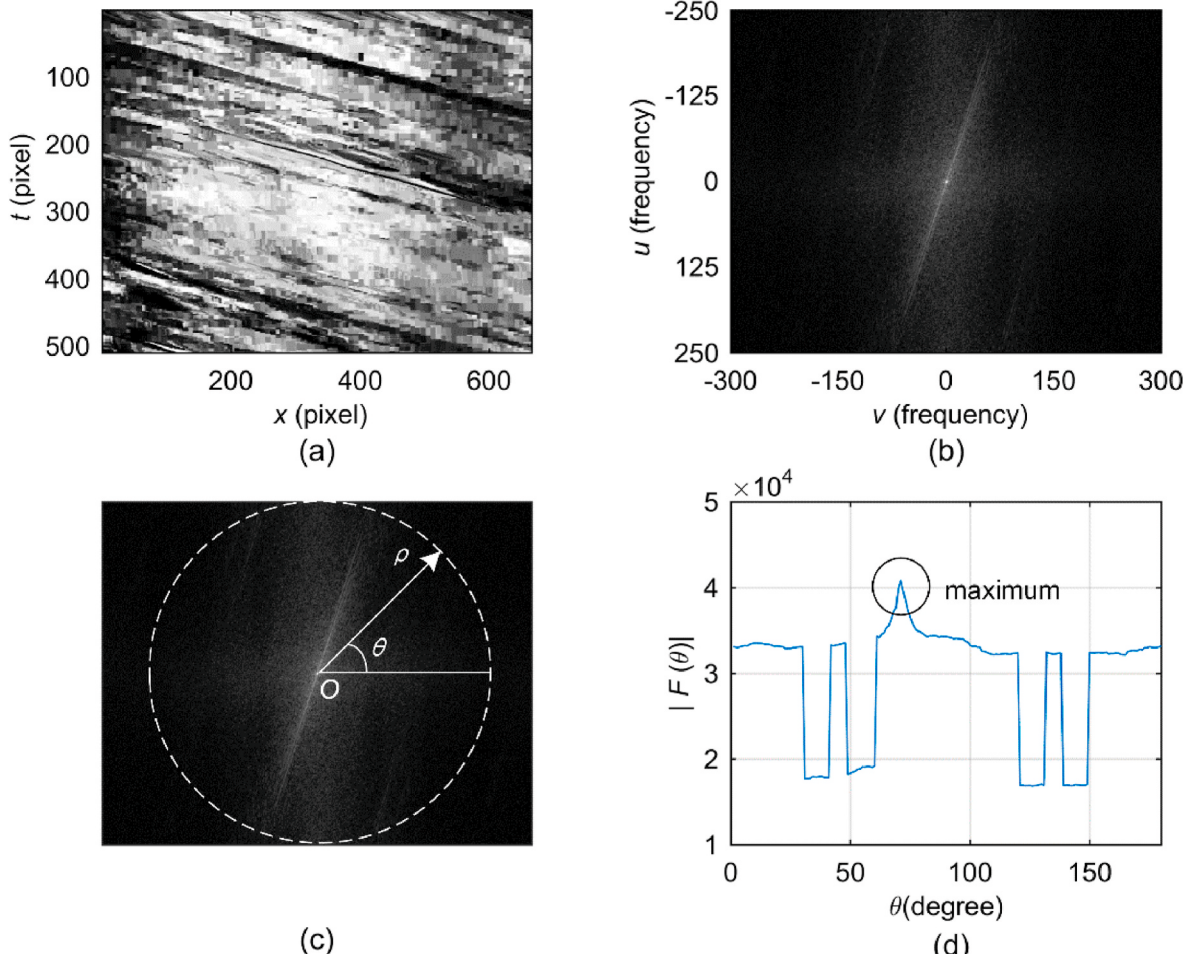


Fig. 10. Detection of the principal direction of the Fourier spectrum. (a) the original STI in the spatial domain. (b) the Fourier spectrum of the processed STI in the frequency domain. (c) the polar coordinate system of (b). (d) the integral spectrum distribution of (c).

removing the noise, the STI is filtered by using the following methods:

A filter in the frequency domain is performed according to Eq. (11), and only the spectrum ranging from $\theta - 4^\circ$ to $\theta + 4^\circ$ is retained to remove the noise interfering with the texture.

$$F'(u, v) = F(u, v) \times J \quad (11)$$

where $F(u, v)$ is the original spectrum, $F'(u, v)$ is the filtered spectrum, and J is the filter.

This process is illustrated clearly in Fig. 12.

3.4. Get the noiseless STI

The filtered spectrum is converted back into the spatial domain by using the 2-D inverse discrete Fourier transform (IDFT, see Eq. (12)), and the filtered STIs and their edge detection results are shown in Figs. 13 and 14 respectively.

$$f(x, y) = \frac{1}{MN} \sum_{x=0}^{M-1} \sum_{y=0}^{N-1} F(u, v) \exp \left[j2\pi \left(\frac{ux}{M} + \frac{vy}{N} \right) \right] \quad (12)$$

where all symbols have the same meaning as in Eq. (7).

It is worth noting that with such a noiseless image, satisfactory results can be obtained no matter what kind of texture detection algorithm is used.

3.5. Summary

The new algorithm overcomes the shortcomings of the previous methods and can accurately obtain the texture of the STIs in various application scenarios, including various adverse scenarios. The whole process of the improved STIV and the new denoising algorithm is shown in Fig. 15. According to the steps in Fig. 15, the real-time monitoring of the river surface velocity and the cross-sectional discharge can be realized.

4. Comparative experiment

4.1. Outline of the experiment

In China's current hydrological measurement system, the velocity and discharge measured by the current meter are regarded as the true value, which is the standard to evaluate the accuracy of various new flow measurement methods. So, to examine the performance of the new denoising algorithm, a comparative experiment was conducted at the Chongyang hydrological station with the impellor-type current meter on June 14, 2019. The Chongyang hydrological station is located on the bank of the Lushui River, a tributary of the Yangtze River. This hydrological station belongs to the Hydrological Bureau of the Yangtze River Water Conservancy Commission and is the state's basic hydrological station.

The experiment was conducted by shooting video images by using a camera from the right bank during a windless period. During the video

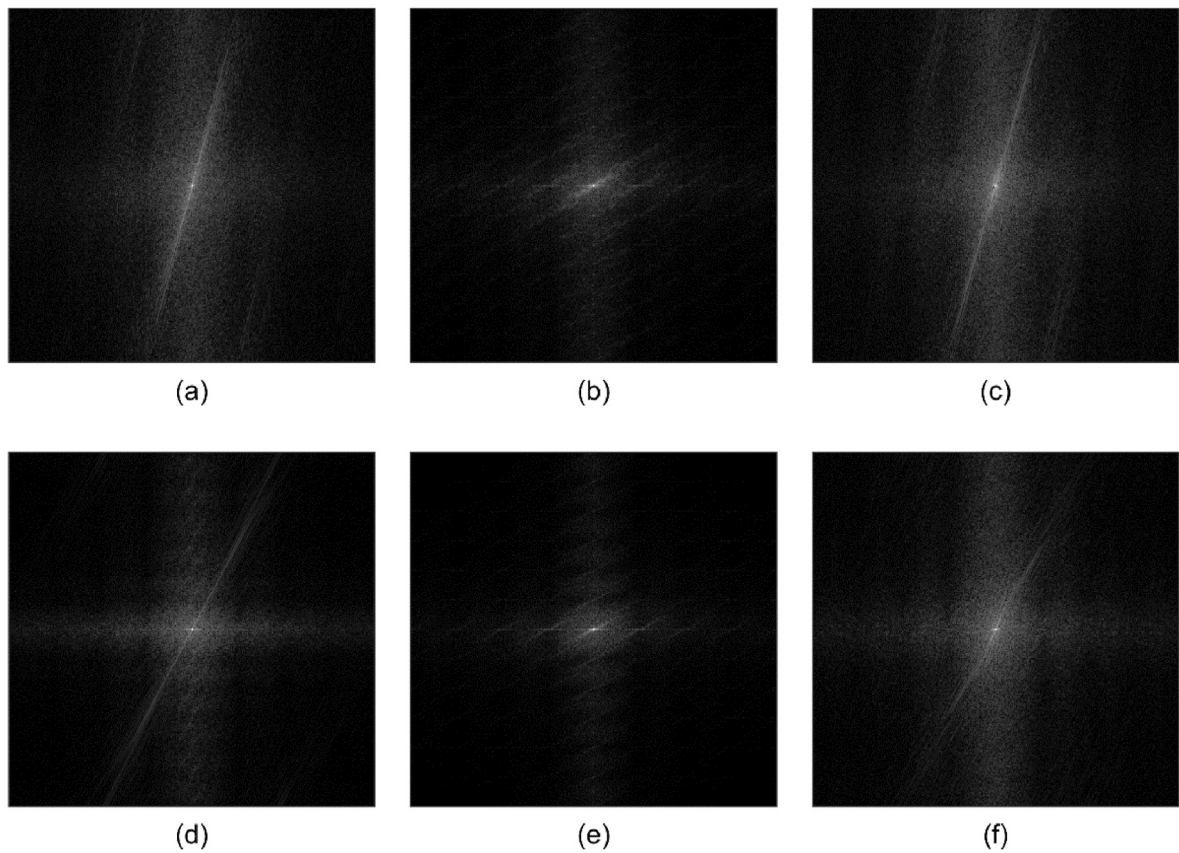


Fig. 11. The Fourier spectrums of the processed STIs in the frequency domain. (a) normal. (b) obstacle. (c) wave. (d) shadow. (e) light. (f) rain.

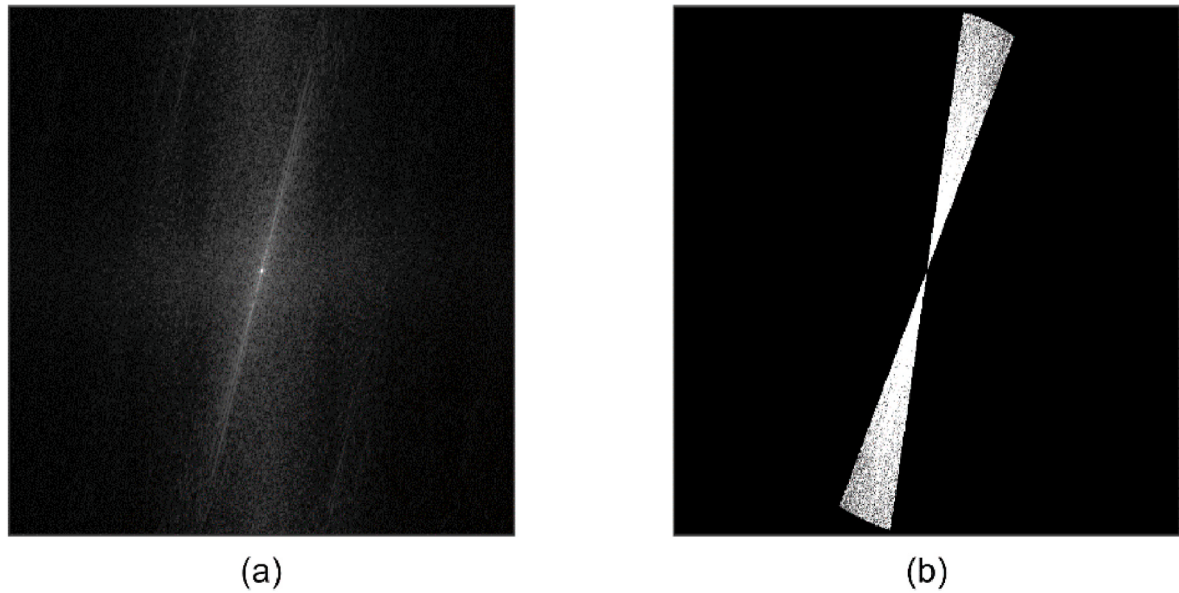


Fig. 12. Filtering in the frequency domain. (a) the spectrum of the processed STI (normal case). (b) the filter in the frequency domain. In (b), the black part represents the spectrum that is filtered out, and the white part is the spectrum that is retained.

shooting, measurement by using an impellor-style current meter was concurrently conducted to ensure that they measured the water flow at the same time. When using the current meter method to measure the flow, the measuring vertical lines were set at 70 m, 80 m, 90 m, 100 m, 110 m, 130 m, and 140 m away from the starting point respectively, and measured the surface velocity and the velocity at the relative depth (the ratio between the depth of the measuring point and the depth of the

vertical line) of 0.2 and 0.8 of each vertical line. According to the position of the current meter in the video image, the velocity-measuring lines were set with equal length at the same positions as the current meter. The surface velocities were calculated by using the original DTM, QESTA, and FFT, as well as the DTM, the QESTA, and the FFT combined with the new denoising algorithm. The experiment site is shown in Fig. 16.

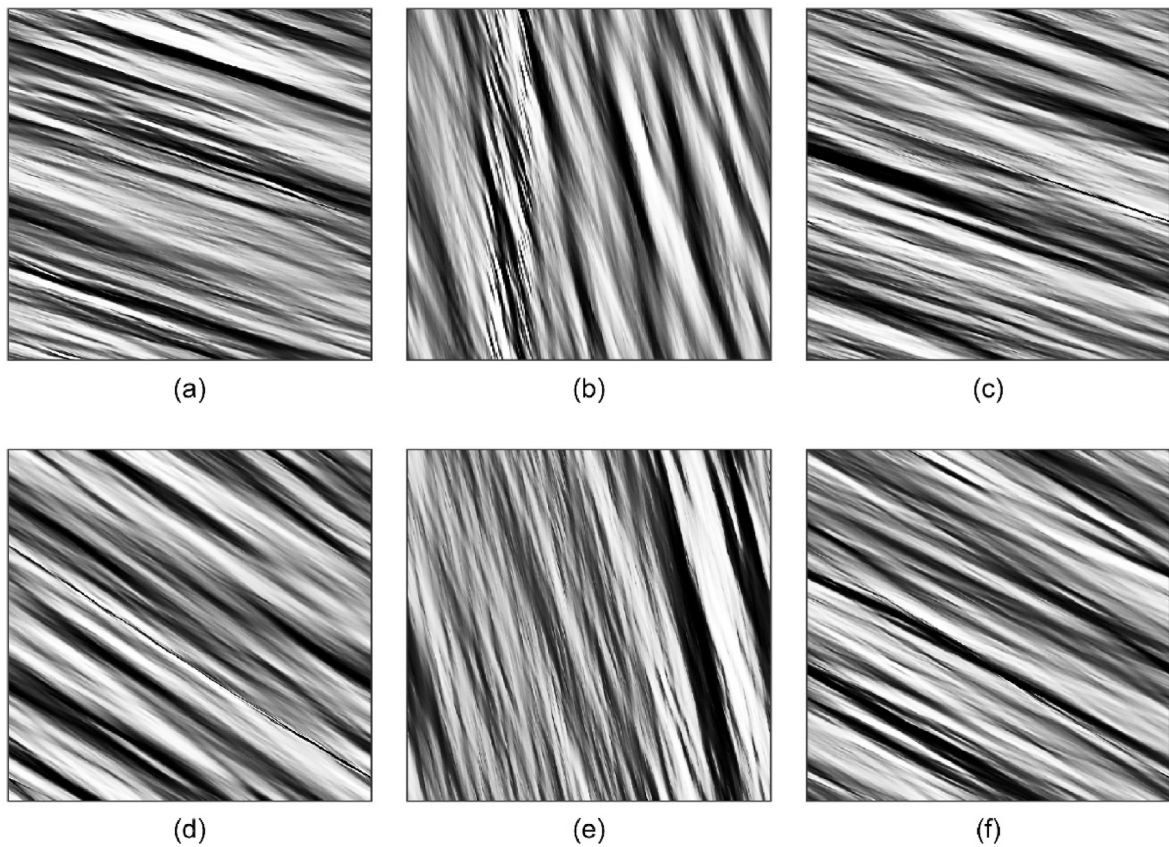


Fig. 13. STIs obtained by using the new denoising method. (a) normal. (b) obstacle. (c) wave. (d) shadow. (e) light. (f) rain.

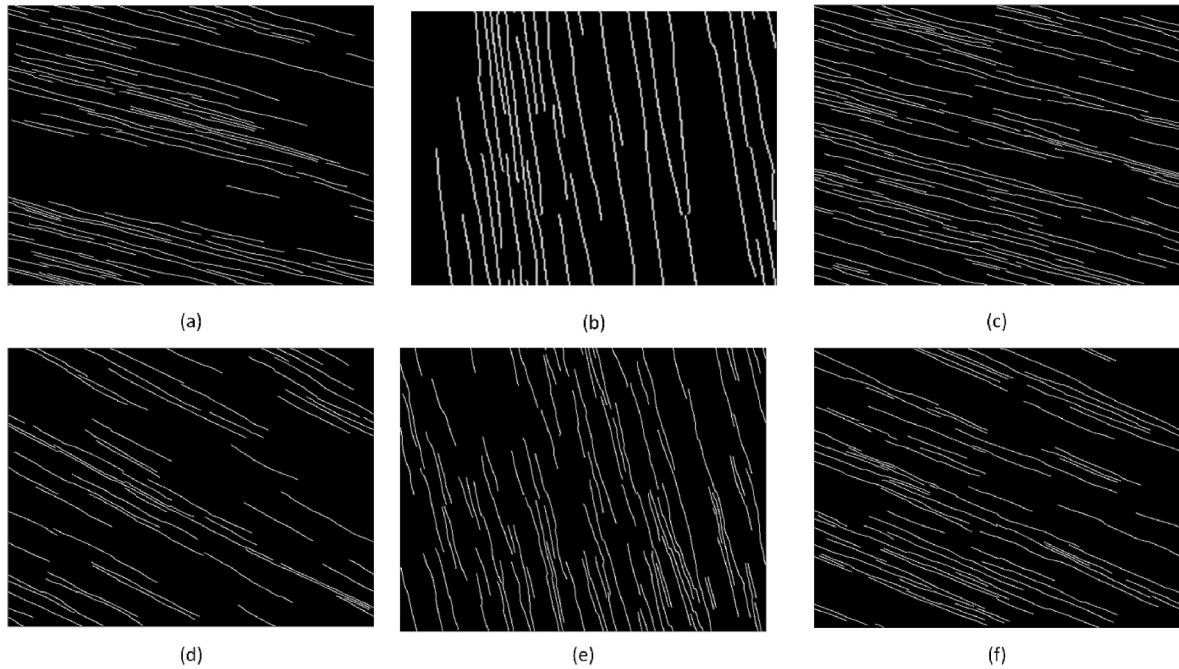


Fig. 14. Edge detection results of the filtered STIs in six cases. (a) normal. (b) obstacle. (c) wave. (d) shadow. (e) light. (f) rain.

4.2. Results

4.2.1. Surface velocity distribution

Table 4 provides the surface velocity and the depth-averaged velocity of each vertical line obtained through the current meter. The

depth-averaged velocity was calculated by the velocities at the relative depth of 0.2 and 0.8 of each vertical line.

Table 5 provides the original STIs of velocity-measuring lines, the STIs with the STD filter, and the STIs processed by the new denoising method.

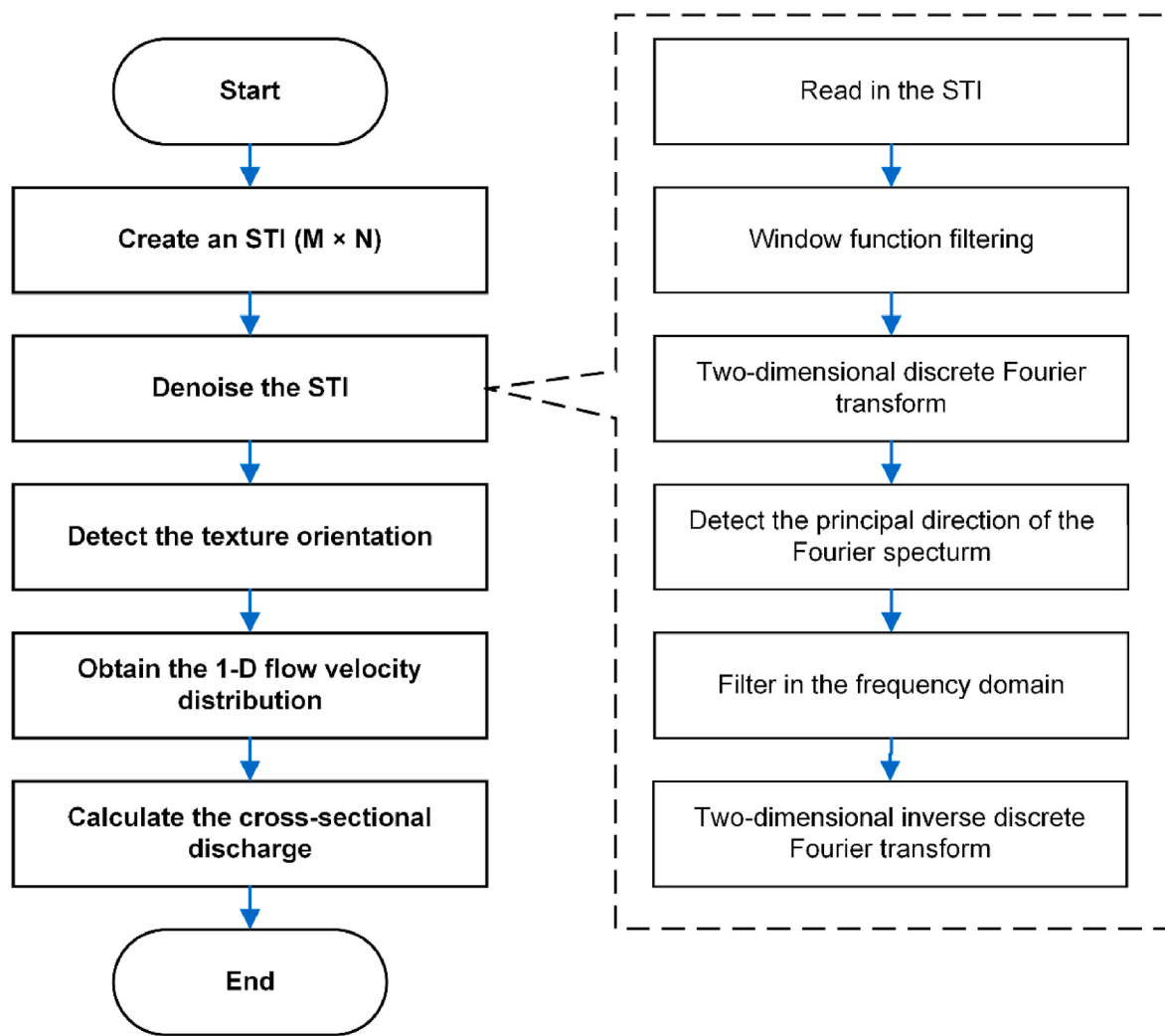


Fig. 15. The whole process of the improved STIV and the new denoising algorithm.



Fig. 16. The experiment fields. The black straight lines represent the velocity-measuring lines, and the red rectangles represent the ground control points. (For interpretation of the references to colour in this figure legend, the reader is referred to the Web version of this article.)

Table 6 provides the edge detection results of the original STIs and the STIs processed by the new denoising method.

Table 7 provides the MOTs and surface velocities (v) obtained by the

original GTM, QUESTA, DFT, and the DTM, QUESTA, FFT combined with the new denoising algorithm. The relative errors (RE) of these methods are also provided. The size of the window used in the GTM is 40 pixels

Table 4

Results of the current meter measurement.

Vertical line	Distance (m)	Surface velocity (m/s)	Depth-averaged velocity (m/s)
No.1	70	0.54	0.395
No.2	80	0.67	0.530
No.3	90	0.69	0.580
No.4	100	0.63	0.515
No.5	110	0.53	0.440
No.6	130	0.51	0.410
No.7	140	0.35	0.205

and the intensification coefficient M used in the QESTA is 15.

4.2.2. Discharge

According to the data measured by the current meter in [Table 4](#), the cross-sectional discharge is calculated by the velocity-area method, as

Table 5

The STIs of velocity-measuring lines.

Velocity-measuring line	Distance(m)	STI (Original)	STI (STD filter)	STI (new denoising method)
No.1	70			
No.2	80			
No.3	90			
No.4	100			
No.5	110			
No.6	130			
No.7	140			

shown in [Table 8](#).

As can be seen from [Table 8](#), the sectional discharge obtained by the current meter method is $59.78 \text{ m}^3/\text{s}$.

Because of its best performance, the surface velocities obtained by the FFT combined with the denoising algorithm are used to calculate the cross-sectional discharge. According to the actual situation of the Chongyang hydrological station and [Table 1](#), $\eta_s = 0.75\text{--}0.8$ is selected, and the calculation results are shown in [Fig. 17](#).

[Table 9](#) shows the process of calculation when η_s is 0.80. When it takes other values, the discharge is calculated in the same way.

As can be seen from [Table 9](#), the sectional discharge is $61.53 \text{ m}^3/\text{s}$ when $\eta_s = 0.80$.

4.3. Discussions

To show the calculation results obtained by different methods more

Table 6
Edge detection results of the STIs.

Velocity-measuring line	Resolution(cm/pixel)	Edge detection of the original STI	Edge detection of the filtered STI
No.1	3.2182		
No.2	3.5379		
No.3	3.8467		
No.4	4.2528		
No.5	4.731		
No.6	5.1253		
No.7	5.3438		

clearly, all the results are plotted in Fig. 18. Fig. 18 provides surface velocity distributions obtained by various techniques: the impellor-style current meter, the original GTM, QESTA, and DFT, as well as the DTM, the QESTA, and the FFT combined with the new denoising algorithm. As can be seen from Fig. 16, houses and trees on the other side of the river result in a large area of reflection on the water surface, thus introducing a lot of noise and interference texture into the STIs. Because of their ineffectiveness in dealing with these low-quality STIs, the relative errors of the original GTM, QESTA, and FFT are up to 348%, 46%, and 97%.

After using the denoising method, the relative errors of the three algorithms are controlled within 23%, 7%, and 6%, respectively, and the calculation accuracy is significantly improved. Compared with the surface velocity data obtained by other methods, the FFT combined with the denoising method produces a favorable velocity distribution which agrees well with the current meter data. Besides, due to the parameter uncertainty of the GTM and the QESTA, the FFT combined with the denoising method has the best performance.

It can be seen from Fig. 18 that the surface velocities obtained by the

Table 7
Results of the experiment.

(a) GTM						
Velocity-measuring line	Original GTM			GTM with new denoising method		
	MOT (°)	v (m/ s)	RE	MOT (°)	v (m/ s)	RE
No.1	43.5	0.92	69.66%	33.1	0.63	16.55%
No.2	44.1	1.03	53.51%	35.4	0.75	12.58%
No.3	48.3	1.30	87.71%	32.3	0.73	5.73%
No.4	41.1	1.11	76.66%	29	0.71	12.26%
No.5	43.2	1.33	151.47%	23.4	0.61	15.88%
No.6	40.6	1.32	158.41%	20.3	0.57	11.52%
No.7	44.4	1.60	348.55%	15	0.43	22.73%

(b) QESTA						
Velocity-measuring line	Original QESTA			QESTA with new denoising method		
	MOT (°)	v (m/ s)	RE	MOT (°)	v (m/ s)	RE
No.1	32.7	0.62	14.78%	30.8	0.58	6.58%
No.2	36.4	0.78	16.79%	33	0.69	2.87%
No.3	36	0.84	21.51%	31.5	0.71	2.49%
No.4	30.9	0.76	21.20%	27.1	0.65	3.63%
No.5	28.1	0.76	42.99%	21	0.54	2.80%
No.6	15.8	0.44	-14.69%	18.7	0.52	2.05%
No.7	6.7	0.19	-46.19%	13	0.37	5.75%

(c) FFT						
Velocity-measuring line	Original FFT			FFT with new denoising method		
	MOT (°)	v (m/ s)	RE	MOT (°)	v (m/ s)	RE
No.1	40.9	0.84	54.87%	30	0.56	3.22%
No.2	20.6	0.40	-40.46%	32.5	0.68	0.92%
No.3	25.4	0.55	-20.58%	31.1	0.70	0.89%
No.4	8.1	0.18	-71.18%	26.6	0.64	1.41%
No.5	0.6	0.01	-97.20%	20.8	0.54	1.72%
No.6	0.5	0.01	-97.37%	19	0.53	3.81%
No.7	0.5	0.01	-96.00%	13	0.37	5.75%

Table 8
Calculation of the discharge based on the current meter measurement.

Section number	Partial area (m ²)	Average velocity in the partial area(m/s)	Partial discharge (m ³ /s)
1	16.42	0.28	4.54
2	12.25	0.46	5.67
3	14.90	0.56	8.27
4	16.60	0.55	9.09
5	18.70	0.48	8.93
6	41.50	0.43	17.64
7	16.50	0.31	5.07
8	4.02	0.14	0.58

GTM, QESTA, and FFT combined with the denoising method are all larger than those measured by the current meter. Actually, to eliminate the influence of flow pulsation and ensure the stability of the measured value, the impellor of the current meter must be placed at least 20 cm below the water surface. So, the surface velocities measured by the current meter are not the real values, which are only approximately considered as the surface velocities. Therefore, it is reasonable that the velocities obtained by these methods are larger than those measured by the current meter. In addition, because the surface velocity is small (less than 1 m/s), the influence of wind on the surface velocity cannot be ignored, and the influence of wind may also be one of the reasons for the larger surface velocities. Finally, it can be seen from Table 7 that the relative errors of the calculation results tend to increase with the decrease of the resolution of the velocity-measuring line, which

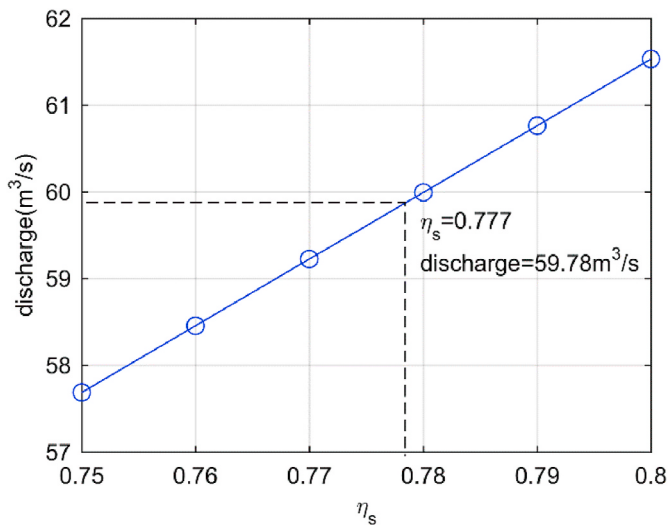


Fig. 17. Result of the discharges with different η_s .

Table 9

Calculation of the discharge based on the FFT combined with the new denoising algorithm ($\eta_s = 0.8$).

Section number	Partial area (m ²)	Average velocity in the partial area(m/s)	Partial discharge (m ³ /s)
1	16.42	0.31	5.13
2	12.25	0.49	6.04
3	14.90	0.55	8.18
4	16.60	0.53	8.86
5	18.70	0.47	8.81
6	41.50	0.43	17.74
7	16.50	0.36	5.94
8	4.02	0.21	0.83

indicates that the width of the river that the current STIV can be applied cannot exceed a certain range. When the width exceeds a certain value, the spatial resolution of the velocity-measuring line far away from the camera will be very low, which affects the accuracy of the measurement.

As for the discharge data, as shown in Fig. 17, when $\eta_s = 0.75$, the discharge is $57.69 \text{ m}^3/\text{s}$, with a relative error of -3.50%. When $\eta_s = 0.8$, the discharge is $61.53 \text{ m}^3/\text{s}$, and the relative error is 2.93%. When η_s is 0.777, the same discharge value as the current meter method can be obtained. The estimated discharges obtained from the surface velocity distribution are all within a reasonable range. Therefore, if the reasonable surface velocity coefficient is selected according to the river conditions, satisfactory discharge data can be obtained by the improved STIV.

5. Conclusions

The STIV is recognized as a promising technique in real-time monitoring of river flow, because measurements can be executed safely, conveniently, and efficiently by analyzing river surface images captured from the river bank. What should be noted in this image analysis method is that many river monitoring cameras (CCTVs, webcams, etc.) are provided directly in each river as an infrastructure for disaster prevention, and this greatly reduces the cost of using the STIV. However, in the previous algorithms, due to the poor image quality and the defects of the algorithms themselves, the calculation results were biased or distorted, which seriously limited the promotion and the use of the STIV. To improve the reliability of the STIV measurement, a new denoising method that generates almost noiseless STIs with clear texture is developed and combined with existing texture detection algorithms. The new method can obtain good results even under bad shooting

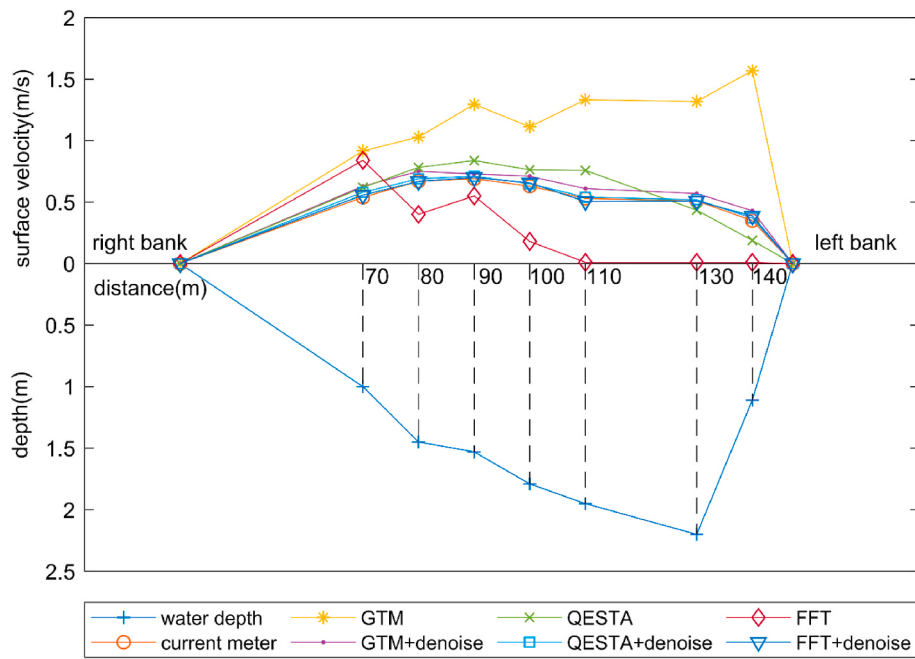


Fig. 18. Comparison of surface velocity distributions of different methods.

conditions, and it greatly improves the robustness of the STIV. In the subsequent comparative experiment, the surface velocity distribution and the sectional discharge obtained by the improved STIV are still in good agreement with the measured results of the current meter, even if the previous methods are ineffective. Besides, the FFT-based STIV performs best in these three improved algorithms. The relative errors of the surface velocities are controlled within 6%, and the relative errors of the discharges are controlled within $\pm 4\%$. Even there are still some problems that need to be further studied in the STIV method, such as the influence of the wind, the limitation of the river width, the length of the velocity-measuring line, etc., but the STIV with the new denoising method has the preliminary application ability and a real-time flow monitoring system can be easily constructed. The hydraulic information obtained by such a monitoring system, together with other hydrologic data, would be of great help in the efficient management of river basins.

Credit author statement

Haoyuan Zhao: Methodology, Software, Investigation, Writing - Original Draft, Visualization, **Hua Chen:** Conceptualization, Writing - Review & Editing, Supervision, Funding acquisition, **Bingyi Liu:** Conceptualization, Project administration, **Weigao Liu:** Software, Validation, Investigation, **Chong-Yu Xu:** Writing - Review & Editing, **Shenglian Guo:** Funding acquisition, **Jun Wang:** Resources.

Declaration of competing interest

The authors declare that they have no known competing financial interests or personal relationships that could have appeared to influence the work reported in this paper.

Acknowledgments

This work was supported by the National Key Research and Development Program (2019YFC1510602). The experiment site and data were provided by the Hydrological Bureau of the Yangtze River Water Conservancy Commission. The authors are grateful for their support of this study.

References

- [1] S. Quirin, Increased flood risk linked to global warming, *Nature* 470 (7334) (2011) 316.
- [2] G. Heritage, et al., Quantifying and contextualising cyclone-driven, extreme flood magnitudes in bedrock-influenced dryland rivers, *Adv. Water Resour.* 123 (2019) 145–159.
- [3] M. Convertino, A. Annis, F. Nardi, Information-theoretic portfolio decision model for optimal flood management, *Environ. Model. Software* 119 (2019) 258–274.
- [4] D. Lee, P. Ward, P. Block, Attribution of large-scale climate patterns to seasonal peak-flow and prospects for prediction globally, *Water Resour. Res.* 54 (2) (2018) 916–938.
- [5] S.E. Rantz, Measurement and computation of streamflow, USGS Water Supply Paper 2175 (1) (1982) 313.
- [6] Y.C. Chen, Flood discharge measurement of mountain rivers, *Hydrol. Earth Syst. Sci. Discuss.* 9 (11) (2012) 12655–12690.
- [7] R.L. Gordon, Acoustic measurement of river discharge, *J. Hydraul. Eng.* 115 (7) (1989) 925–936.
- [8] I. Fujita, M. Muste, A. Kruger, Large-scale particle image velocimetry for flow analysis in hydraulic engineering applications, *J. Hydraul. Res.* 36 (3) (1998) 397–414.
- [9] K.T. Holland, et al., Practical use of video imagery in nearshore oceanographic field studies, *IEEE J. Ocean. Eng.* 22 (1) (1997) 81–92.
- [10] I. Fujita, S. Aya, Refinement of LSPIV technique for monitoring river surface flows, in: ASCE 2000 Joint Conference on Water Resources Engineering and Water Resources Planning & Management, 2000, pp. 1–9. Minneapolis.
- [11] A. Hauet, J. Creutin, P. Belleudy, Sensitivity study of large-scale particle image velocimetry measurement of river discharge using numerical simulation, *J. Hydrol.* 349 (1–2) (2008) 178–190.
- [12] M. Jodeau, et al., Application and evaluation of LS-PIV technique for the monitoring of river surface velocities in high flow conditions, *Flow Meas. Instrum.* 19 (2) (2008) 117–127.
- [13] M. Muste, I. Fujita, A. Hauet, Large-scale particle image velocimetry for measurements in riverine environments, *Water Resour. Res.* 44 (4) (2008).
- [14] J. Le Coz, et al., Performance of image-based velocimetry (LSPIV) applied to flash-flood discharge measurements in Mediterranean rivers, *J. Hydrol.* 394 (1–2) (2010) 42–52.
- [15] M. Lee, et al., The measurement of discharge using a commercial digital video camera in irrigation canals, *Flow Meas. Instrum.* 21 (2) (2010) 150–154.
- [16] M. Muste, et al., Capabilities of large-scale particle image velocimetry to characterize shallow free-surface flows, *Adv. Water Resour.* 70 (2014) 160–171.
- [17] K. Yu, S. Kim, D. Kim, Correlation analysis of spatio-temporal images for estimating two-dimensional flow velocity field in a rotating flow condition, *J. Hydrol.* 529 (2015) 1810–1822.
- [18] A. Stumpf, et al., Photogrammetric discharge monitoring of small tropical mountain rivers: a case study at Rivière des Pluies, Réunion island, *Water Resour. Res.* 52 (6) (2016).
- [19] Z. Chen, et al., River surface target enhancement and background suppression for unseeded LSPIV, *Flow Meas. Instrum.* 30 (30) (2013) 99–111.
- [20] C.C. Chickadel, R.A. Holman, M.H. Freilich, An optical technique for the measurement of longshore currents, *J. Geophys. Res.* 108 (C11) (2003).

- [21] I. Fujita, H. Watanabe, R. Tsubaki, Development of a non-intrusive and efficient flow monitoring technique: the space-time image velocimetry (STIV), *Int. J. River Basin Manag.* 5 (2) (2007) 105–114.
- [22] R. Tsubaki, I. Fujita, S. Tsutsumi, Measurement of the flood discharge of a small-sized river using an existing digital video recording system, *J. Hydro Environ. Res.* 5 (4) (2011) 313–321.
- [23] I. Fujita, Discharge measurements of snowmelt flood by space-time image velocimetry during the night using far-infrared camera, *Water* 9 (4) (2017) 269.
- [24] I. Fujita, et al., Spatial measurements of snowmelt flood by image analysis with multiple-angle images and radio-controlled ADCP, *J. JSCE* 5 (1) (2017) 305–312.
- [25] I. Fujita, et al., Efficient and Accurate Estimation of Water Surface Velocity in STIV, *Environmental Fluid Mechanics*, 2018.
- [26] Z. Zhen, et al., Design and evaluation of an FFT-based space-time image velocimetry (STIV) for time-averaged velocity measurement, in: 14th IEEE International Conference on Electronic Measurement & Instruments (ICEMI). 2019, 2019.
- [27] C. Liu, et al., Bundle adjustments CCD camera calibration based on collinearity equation, *Chin. J. Mech. Eng.* 17 (4) (2004) 494–497.
- [28] R.C. Gonzalez, R.E. Woods, *Digital Image Processing*, third ed. ed, Publishing House of Electronics Industry, Beijing, 2010.
- [29] Y. Wu, Q. Yu, Translation estimation by phase-shifting of Fourier transform, *Opto-Electronic Eng.* 32 (8) (2005) 73–76.